PCCP

PAPER

View Article Online
View Journal | View Issue

Cite this: *Phys. Chem. Chem. Phys.*, 2018, **20**, 22563

A rechargeable aluminum-ion battery based on a VS_2 nanosheet cathode†

Lu Wu, Ruimin Sun, Fangyu Xiong, Cunyuan Pei, Kang Han, Chen Peng, Yuqi Fan, Wei Yang, Qinyou An* and Liqiang Mai*

Received 27th July 2018,
Accepted 21st August 2018

DOI: 10.1039/c8cp04772c

rsc.li/pccp

As a typical member of transition-metal dichalcogenides (TMDs), VS_2 has been evaluated as the aluminum-ion battery cathode for the first time. To further improve their stability and conductivity, the as-prepared VS_2 nanosheets are modified with graphene (denoted as G-VS_2). And the G-VS_2 electrode delivers a high initial discharge capacity of 186 mA h g^{-1} at 100 mA g^{-1} with almost 100% coulombic efficiency after 50 cycles. Furthermore, an explicit intercalation mechanism of Al into G-VS_2 has been investigated by *in/ex situ* XRD, *ex situ* Raman and TEM spectroscopy. And the G-VS_2 composite proves to be an impressive cathode material for aluminum-ion batteries (AIBs). This work might put forward the application of TMDs in AIBs.

Introduction

Along with the increase of world energy consumption and fossil fuel exhaustion, exploring sustainable energy sources to meet drastic demand is urgently needed.[1–5] Developing large-scale energy storage systems is crucial for the transformation of sustainable energy into electric energy infrastructures.[6–10] New types of multivalent ion batteries, such as Mg-ion batteries (MIBs),[11,12] Zn-ion batteries (ZIBs),[13,14] and Al-ion batteries (AIBs),[15–18] have received considerable attention derived from the abundance and safety of the corresponding metal anodes. Aluminum is the cheapest metal ($\sim$1.4 USD kg^{-1}) due to the largest reserve (82 000 ppm in the earth's crust) when compared with other multivalent metal anodes.[16] Moreover, trivalent charge carriers can provide high volumetric capacity (8046 mA h cm^{-3}) and gravimetric capacity (2980 mA h g^{-1}).[19] Despite the above advantages, long-standing challenges still limit the development of AIBs. The major obstacle comes from the inherently strong polarization effect between Al^{3+} and the framework lattice of the cathode material, which could increase the diffusion resistance and limit the specific capacity.[11,20] Thus, finding suitable cathode materials becomes the formidable challenge for AIBs.[21]

The preliminary exploration of cathode materials mostly focused on V_2O_5.[19,22,23] However, such intercalation-type cathodes still confront the main bottlenecks of rapid capacity fading and limited cycle life, possibly resulting from incompatibility with the oxide anionic framework because of their strong electrostatic interactions.[23] Carbon-based materials are other typical intercalation-type cathodes, which can deliver high-rate capacities.[17,24–26] But the intercalation of the complex ion group $AlCl_4^-$ instead of Al^{3+} and the lower theoretical capacity ($\approx$100 mA h g^{-1} for graphite) for these types of materials will overshadow the reachable capacity. Recently, transition metal sulfides have received significant attention in AIBs for their excellent characteristics.[27–30] In particular, typical members of TMD cathode materials, such as SnS_2,[31] TiS_2[32] and MoS_2,[33] can also be considered as ideal cathode materials for AIBs, owing to more active sites to accommodate cations.[34] In addition, the framework has also a lower electronegativity and a higher polarizability, resulting in facility for Al^{3+} intercalation and extraction. VS_2 is the typical member of TMDs with high specific theoretical capacity relied on multiple oxidation states of rich chemical valences in vanadium and sulfide.[35,36] Besides, the VS_2 crystal can exhibit a sandwich structure consisting of a vanadium layer between two sulfur layers. The interlayer space of VS_2 is 5.76 Å, which is enough to enable the convenient intercalation/de-intercalation of Al^{3+} ions (ionic diameter: 0.59 Å). Therefore, VS_2 has great potential as a cathode material candidate for AIBs.

Herein, we demonstrate rechargeable AIBs using VS_2 nanosheets as the cathode material. To achieve better electrochemical performance of VS_2, graphene is used to modify VS_2, which delivers a high initial discharge capacity of 186 mA h g^{-1} at 100 mA g^{-1}. Additionally, in the cycling process, the retention of discharge capacity could remain at 50 mA h g^{-1} with a coulombic efficiency of approximately 100% after 50 cycles. Furthermore, advanced *in/ex situ* X-ray diffraction (XRD), *ex situ* high-resolution transmission electron microscopy (HRTEM) and Raman spectroscopy have been utilized to reveal the reaction mechanism of G-VS_2 acting as a novel cathode material for AIBs.

State Key Laboratory of Advanced Technology for Materials Synthesis and Processing, Wuhan University of Technology, Wuhan 430070, Hubei, China. E-mail: anqinyou86@whut.edu.cn, mlq518@whut.edu.cn

† Electronic supplementary information (ESI) available: SEM, elemental analysis of C, H, N, and S and electrochemical properties. See DOI: 10.1039/c8cp04772c

Experimental

Synthesis of VS_2

Firstly, 0.232 g NH_4VO_3 was dispersed in 30 mL deionized water, at the same time, 2 mL $NH_3{\cdot}H_2O$ (Aladdin, 28–30%) was slowly added under continuous stirring. Next, 1.503 g thioacetamide (TAA) was dispersed in the solution accompanied by continuous stirring. Finally, a homogeneous brown solution was obtained. After that, the mixture was transferred into a 50 mL Teflon-lined sealed autoclave and maintained at 180 °C for 20 h. By cooling down to natural temperature, the suspension was washed several times with ethanol and distilled water. The final black powder was obtained *via* drying at 60 °C for 8 h in a vacuum oven.

Synthesis of G-VS_2

To obtain graphene-modified VS_2, 0.1 g VS_2 was added in deionized water and stirred for 30 min. Next, 0.89 mL graphene solution ($\approx$12.6 mg mL^{-1}) was dispersed in the former suspension solution using ultrasonic treatment by vigorously mixing for 6 h. Graphene was synthesized by a modified Hummers method.[37] The final composition powder was obtained by centrifuging and drying at 60 °C for 8 h in the vacuum oven.

Materials characterization

The XRD patterns were obtained by using a D8 Advance Discovery X-ray diffractometer with a Cu Kα X-ray source. Field emission scanning electron microscopy (FESEM) images and energy-dispersive X-ray spectra (EDS) were recorded using a JEOL-7100F microscope. Transmission electron microscopy (TEM) and high-resolution transmission electron microscopy images were collected by using a JEM-2100F microscope. The Renishaw inVia micro-Raman spectroscopy system was employed to obtain the Raman spectra. An Organic Elemental Analyzer (OEA) (Vario EL cube/Vario EL cube) was utilized to detect the carbon weight ratio.

Electrochemical measurements

The electrodes were obtained by mixing active materials, acetylene black and polytetrafluoroethylene (PTFE) at a weight ratio of 6 : 3 : 1. Then the slurry was uniformly mixed, transferred to the roller press and cut into Φ6 mm electrodes. The final electrodes were dried in a vacuum oven at 60 °C for 12 h, and Al foil and glass fiber membranes (GF/D Whatman) were used as the anode and the separator, respectively. The electrolyte was a light-yellow transparent ionic liquid made of aluminum chloride ($AlCl_3$, 99.99% Sigma-Aldrich) and 1-ethyl-3-methylimidazolium chloride ([EMIM]Cl, 98% Sigma-Aldrich) at a mole ratio of 1.3 : 1. The pure graphene electrode was prepared by mixing graphene (90 wt%), polyvinylidene fluoride (PVDF, 10 wt%), then the slurry was coated into Φ8 mm electrodes on Mo foil and dried at 60 °C for 12 h, whose loading density of active material is based on volume and volume fraction. All the components were dried in the vacuum oven to remove the residual water. Swagelok type cell is used to avoid corrosion of the electrolyte in the CR2016-type coin cell, the corrosion resistance is due to the internal material of Teflon instead of stainless steel as the reaction chamber. The electrochemical performance of the AIBs was measured using a VMP3 multichannel electrochemical workstation (Bio-Logic, France).

Results and discussion

The XRD patterns of G-VS_2 and VS_2 are presented in Fig. 1a. All the characteristic peaks of as-modified samples are readily indexed to the hexagonal VS_2 phase and no impurity was detected (Fig. 1a). The Raman spectrum of G-VS_2 is shown in Fig. 1b.

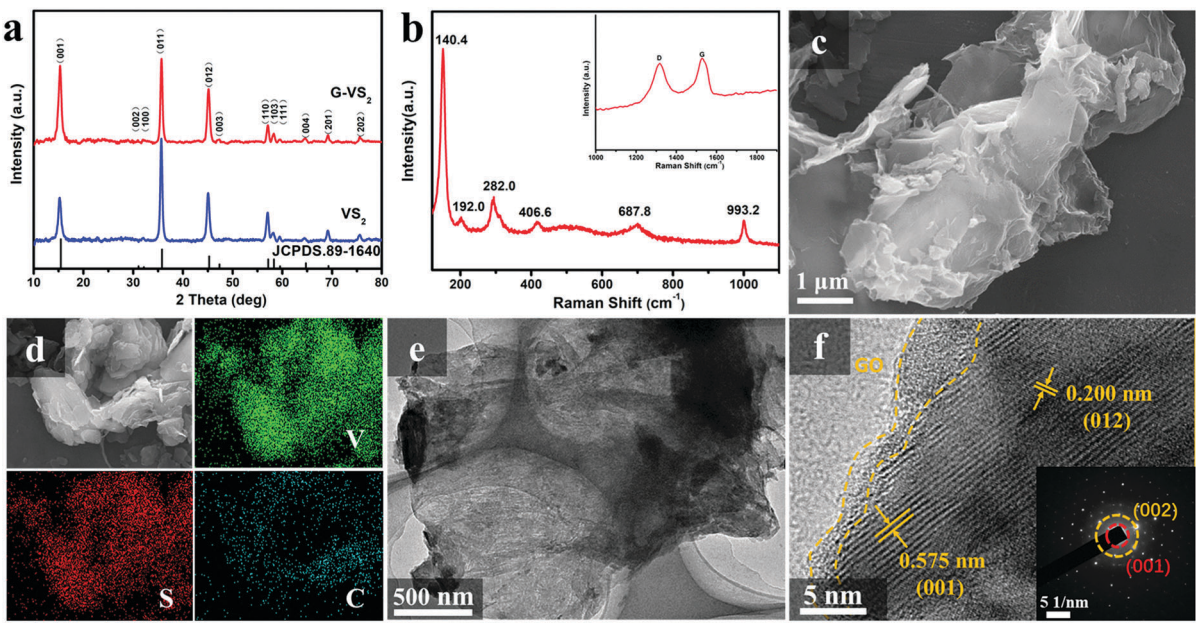

Fig. 1 Structure and characterization of G-VS_2: (a) XRD patterns of G-VS_2 and VS_2. (b) Raman spectra of G-VS_2. (c) SEM image of G-VS_2. (d) The EDS mapping images of G-VS_2. (e) TEM image of G-VS_2. (f) HRTEM and SAED images of G-VS_2.

The D-band (lattice defect in the graphene layer) and the G-band (vibration of the sp^2 hybrid bond in the surface) of graphene are located at nearly 1300 and 1590 cm^{-1}, respectively.[23] Other typical peaks located at 140.4, 192, 282, 406.6, 687.8 and 993.2 cm^{-1} are associated with stretching vibrations and rocking vibrations of V–S bonds.[38] Meanwhile, the carbon content of G-VS_2 is 6.32%, confirmed by organic elemental analysis (Table S1, ESI†). The morphology and structure of G-VS_2 are also investigated by SEM as shown in Fig. 1c. After decorating with graphene, VS_2 microflowers are scattered into nanosheets. Moreover, the energy-dispersive X-ray spectra (EDS) for elemental mapping (Fig. 1d) are employed to detect the elements of V, S and C, and the results reveal that three elements are homogeneously distributed in G-VS_2. The detailed structure of G-VS_2 nanosheets has been further characterized by TEM. A well-defined image of nanosheets decorated with graphene is observed in Fig. 1e. HRTEM analysis (Fig. 1f) further reveals the presence of lattice fringes with spaces of 2.0 Å and 5.75 Å, which can be assigned to the (012) and (001) planes of VS_2, respectively. The selected area electron diffraction pattern shows diffraction rings corresponding to the (001) and (002) planes of the hexagonal phase VS_2.

The electrolyte system plays a vital role in aluminum storage performance, which impacts the reverse reaction stability due to the main ion species ($AlCl_4^-$ and $Al_2Cl_7^-$) in the electrolyte.[39] The stability of the electrolyte was measured using the cyclic voltammogram (CV) at a scan rate of 100 mV s^{-1} in the range of −1 to 2 V. The electrolyte is stable up to 2 V and the coulombic efficiency is close to 100% (Fig. 2a). Polarization of aluminum deposition/dissolution is carried out by galvanostatic measurements at 20 μA cm^{-2} (Fig. S2, ESI†). The overpotential stabilizes at about 0.05 V after the first several cycles. Fig. 2b shows the discharge curves of G-VS_2 and VS_2 at 100 mA g^{-1}. When compared to the initial discharge capacity of VS_2 (145.4 mA h g^{-1}), G-VS_2 achieves a higher capacity of 186 mA h g^{-1}. Specially, the capacity remains at 88.3 mA h g^{-1} in the fifth cycle, while VS_2 exhibits sharp capacity degradation (only 59.4 mA h g^{-1} remains). The CV measurements of the G-VS_2 electrode *vs.* Al^{3+}/Al at a scan rate of 0.2 mV s^{-1} are also shown in Fig. 2c, and the G-VS_2 electrode displays a broad reduction peak and an oxidation peak located at around 0.45 V and 1.6 V in the first cycle, respectively. The redox peak corresponds well with discharge curves. By comparing with the former first few cycles, the G-VS_2 electrode displays stable charge/discharge curves of 10th, 20th and 30th cycles at 100 mA g^{-1} as shown in Fig. 2d, and the enhanced stabilization might be ascribed to the layered structure. The specific reason for the decrease of the capacities in the first several cycles is still unclear, possibly due to the formation of an irreversible solid electrolyte interphase (SEI) or the side reaction.[31] The discharge capacities of the G-VS_2 and VS_2 electrodes at different specific current densities (20, 50, 100, and 200 mA g^{-1}) are shown in Fig. 2e. The capacities of the two cathode materials gradually decrease. However, the G-VS_2 electrode exhibits much better performance than VS_2 at all specific currents. In addition, the G-VS_2 electrode also displays excellent specific capacity at a low current density. The cycling performances and the first three charge–discharge curves are revealed in Fig. S3a–d (ESI†). It can be illustrated that the G-VS_2 electrode could exhibit excellent performance with capacities of 493 mA h g^{-1} and 323 mA h g^{-1} at 20 and 50 mA g^{-1}, respectively. G-VS_2 shows better cycling performance than VS_2. To the best of our knowledge, as a cathode

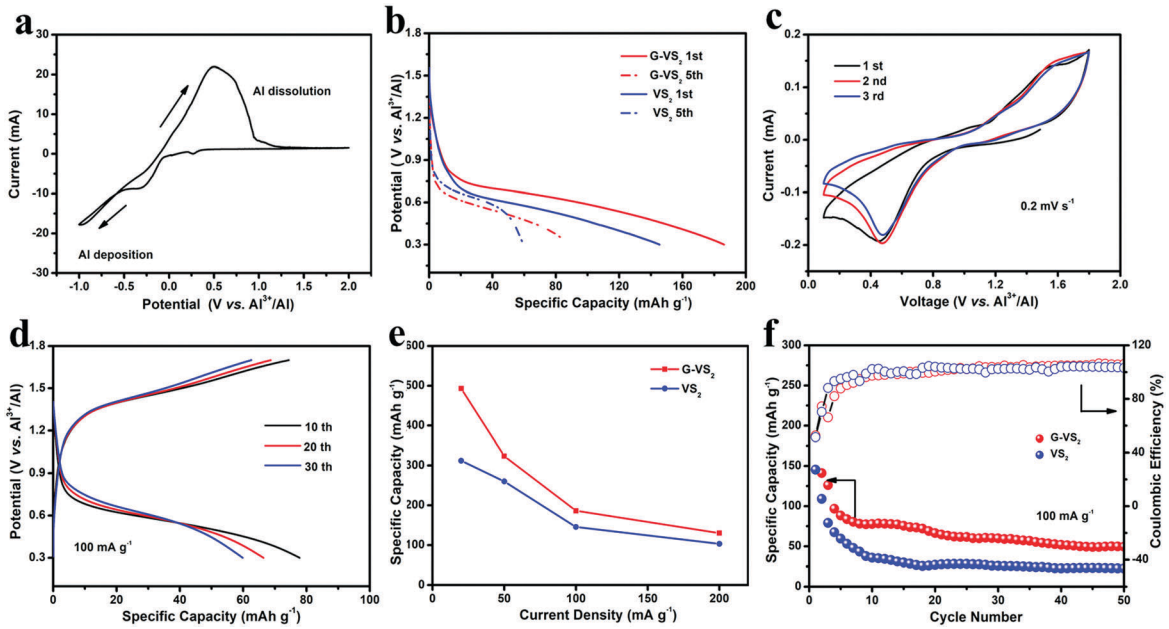

Fig. 2 Electrochemical performances of the VS_2 and G-VS_2 as the cathode materials. (a) Al deposition and dissolution in EMIC : $AlCl_3$ at a mole ratio of 1 : 1.3. (b) The first/fifth discharged curves of VS_2 and G-VS_2 at 100 mA g^{-1}. (c) Cyclic voltammetry curves at 0.2 mV s^{-1}. (d) 10/20/30th charge–discharge curves of G-VS_2 at 100 mA g^{-1}. (e) The discharge capacity of VS_2 and G-VS_2 at different current densities. (f) Comparison of the discharge capacity and coulombic efficiency of VS_2 and G-VS_2 at 100 mA g^{-1}.

material for AIBs, G-VS_2 exhibits a relatively high specific capacity compared to that of the state-of-the-art reported transition metal sulfide (Table S2, ESI†).[27–33,36,40]

The cycling performances at high specific current density were measured and are shown in Fig. 2f, and the G-VS_2 electrode displays a capacity of 50 mA h g^{-1} at 100 mA g^{-1} and the coulombic efficiency approaches to 100% after 50 cycles. However, the capacity of the VS_2 electrode only remains at 22 mA h g^{-1} under the same conditions. As shown in Fig. S4 (ESI†), the pure GO electrode shows negligible capacity at 10 mA g^{-1}. Therefore, the capacity of G-VS_2 mostly comes from VS_2. The remarkable capacity improvement may be ascribed to the synergistic modification of graphene with the layered crystal structure of VS_2, which is regarded as an applicable method to facilitate efficient electronic transport in cathode materials. Electrochemical impedance spectra (EIS) were measured to investigate the electronic conductivity of the two samples (Fig. S5, ESI†). The Nyquist plots show that the charge transfer resistance (R_{ct}) of G-VS_2 is much lower than that of VS_2. These results indicate that the G-VS_2 sample possesses higher electronic conductivity, which may be the main reason of its better performances.

To further investigate the Al deposition/dissolution behavior of the Al metal anode, the SEM images of the Al metal at different charged/discharged states are shown in Fig. S6a–c (ESI†). The rugged morphology corresponds to the dissolution of Al^{3+} from the Al anode and filled holes correspond to the deposition of Al^{3+} ions on the Al metal. It is obvious that the corrosion of the Al anode either chemically or electrochemically has been detected after 50 cycles (Fig. S6d, ESI†). *In/ex situ* XRD and *ex situ* HRTEM are performed to reveal the structural evolution and storage mechanism of G-VS_2 during aluminum insertion and extraction. For the *in situ* XRD, the time-resolved experiment was conducted. Fig. 3a shows the *in situ* XRD patterns during the first two cycles and the corresponding charge–discharge curves. It can be directly observed that two typical peaks located at 15.4° and 35.7° (corresponding to the (001) and (011) planes of VS_2, respectively) gradually weaken during the discharge process. Interestingly, no obvious change is observed during the initial discharge state. When the electrode was discharged from 0.7 to 0.3 V, the peaks distinctly weaken and finally disappear, which is caused by the insertion of Al^{3+}.

Subsequently, the peak centered at 15.4° and 35.7° strengthen in the following charge process, which are caused by the extraction of Al^{3+} and the reinstatement of the crystal structure. The same trend occurs in the second cycle. Moreover, the HRTEM image of G-VS_2 after being fully charged to 1.7 V is displayed in Fig. S7 (ESI†). The evident lattice fringes also demonstrate that G-VS_2 retained good crystallinity, which is in agreement with the *in situ* XRD results, reflecting the recovery of crystallinity during the cycling process. The *ex situ* XRD results provide a further insight into the structural stability of G-VS_2 at various charged and discharged states (Fig. 3b–d). In general, when the electrode was discharged to 0.8 V (state I to state II), no obvious change in the intensity and position of the typical peaks can be detected. However, the intensities of the peaks at 15.4° and 35.7° are gradually decreased from state II to state III. And the peak at

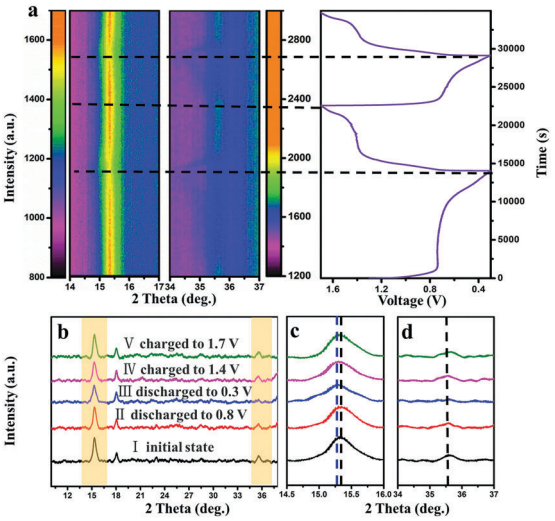

Fig. 3 (a) *In situ* XRD patterns of G-VS_2 and their corresponding charge–discharge curves at 50 mA g^{-1}. (b) *Ex situ* XRD patterns of G-VS_2 at different states. (c and d) Enlargement of the selected regions.

15.4° slightly shifts toward a low angle (Fig. 3c), resulting from the increase of the interlayer space corresponding to the (001) plane. Besides, in contrast, when the electrode was charged to 1.7 V (state V), the peaks move back to their origin position, illustrating that there is no severe structural deterioration in the process of Al^{3+} insertion/extraction. In addition, a similar conclusion is also revealed by the *ex situ* Raman spectra of G-VS_2 at different states (Fig. 4a). No change is observed for the peaks after fully charged and discharged processes, which fits well with the above results. Besides, the EDS mappings of G-VS_2 are displayed after the initial discharge process, which shows that the elements of V, S, C and Al are homogeneously distributed (Fig. 4b). By combining *in/ex situ* XRD, *ex situ* HRTEM and Raman spectroscopy, it can be concluded that the layered structural framework of VS_2 is suitable to tolerate the insertion and extraction of Al^{3+}.

As described above, the electrochemical reaction can be summarized as the following equations:

$$VS_2 + xAl^{3+} + 3xe^- \leftrightarrow Al_xVS_2 \text{ (cathode)}$$

$$Al + AlCl_4^- + 3xe^- \leftrightarrow Al_2Cl_7^- \text{ (anode)}$$

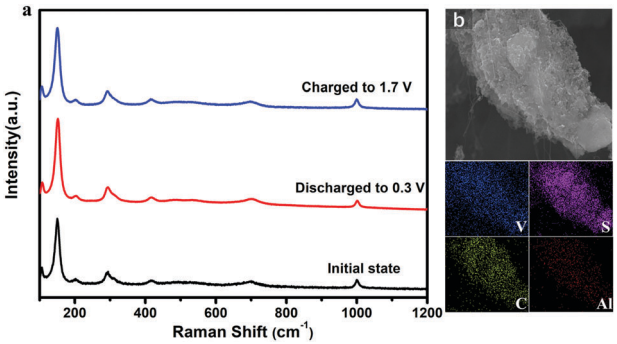

Fig. 4 (a) Raman spectra of G-VS_2 at different states. (b) The EDS mapping images of the G-VS_2 electrode after the fully discharged process.

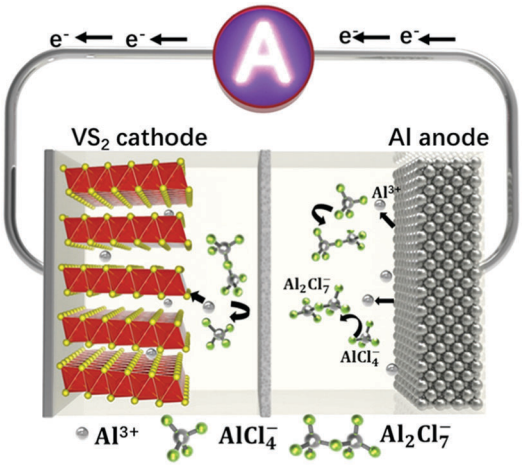

Fig. 5 Schematic illustration of AIBs with G-VS_2 as the cathode during the discharge process.

Hence, the schematic is illustrated in Fig. 5. During the discharge process, Al^{3+} ions insert into the interlayers of VS_2, while metallic Al combines with $AlCl_4^-$ (formation of $Al_2Cl_7^-$). Reversible deposition and dissolution reactions can be observed on the anode side, relying on the composition of the electrolyte ($AlCl_4^-$ and $Al_2Cl_7^-$).[41]

Conclusions

In conclusion, the layered G-VS_2 is successfully synthesized by a convenient physical coating method, and a highly stable framework can be obtained, which is propitious to ion diffusion and faster electron transport and delivers excellent electrochemical performance. An initial discharge capacity of 186 mA h g^{-1} is obtained at 100 mA g^{-1}. Furthermore, the intercalation reaction mechanism has also been proved by *in*/*ex situ* XRD, *ex situ* Raman spectroscopy and HRTEM, indicating that there is a slight structural change during intercalation of Al^{3+}. We believe that this work may highlight the significance of exploring layered TMDs as the cathode material for AIBs.

Conflicts of interest

There are no conflicts to declare.

Acknowledgements

This work was supported by the National Key Research and Development Program of China (2016YFA0202603), the National Natural Science Fund for Distinguished Young Scholars (51425204), the National Natural Science Foundation of China (51521001), the Programme of Introducing Talents of Discipline to Universities (B17034), the Yellow Crane Talent (Science & Technology) Program of Wuhan City, and the International Science & Technology Cooperation Program of China (2013DFA50840).

Notes and references

1 S. Chu and A. Majumdar, *Nature*, 2012, **488**, 294–303.
2 V. Etacheri, R. Marom, E. Ran, G. Salitra and D. Aurbach, *Energy Environ. Sci.*, 2011, **4**, 3243–3262.
3 D. Larcher and J. Tarascon, *Nat. Chem.*, 2015, **7**, 19–29.
4 Y. Wang, J. Zhou, J. Wu, F. Chen, P. Li, N. Han, W. Huang, Y. Liu, H. Ye and F. Zhao, *J. Mater. Chem. A*, 2017, **5**, 25618–25624.
5 G. Li, D. Luo, X. Wang, H. S. Min, S. Hemmati, A. Yu and Z. Chen, *Adv. Funct. Mater.*, 2017, **27**, 1702502.
6 F. Bonaccorso, L. Colombo, G. Yu, M. Stoller, V. Tozzini, A. C. Ferrari, R. S. Ruoff and V. Pellegrini, *Science*, 2015, **347**, 1246501.
7 S. Tepavcevic, H. Xiong, V. R. Stamenkovic, X. Zuo, M. Balasubramanian, V. B. Prakapenka, C. S. Johnson and T. Rajh, *ACS Nano*, 2012, **6**, 530–538.
8 Y. K. Sun, Z. Chen, H. J. Noh, D. J. Lee, H. G. Jung, Y. Ren, S. Wang, C. S. Yoon, S. T. Myung and K. Amine, *Nat. Mater.*, 2012, **11**, 942–947.
9 T. Kennedy, M. Brandon and K. M. Ryan, *Adv. Mater.*, 2016, **28**, 5696–5704.
10 M. Sathiya, A. M. Abakumov, D. Foix, G. Rousse, K. Ramesha, M. Saubanère, M. L. Doublet, H. Vezin, C. P. Laisa and A. S. Prakash, *Nat. Mater.*, 2015, **14**, 230–238.
11 E. Levi, Y. Gofer and D. Aurbach, *Chem. Mater.*, 2010, **22**, 860–868.
12 F. Xiong, Y. Fan, S. Tan, L. Zhou, Y. Xu, C. Pei, Q. An and L. Mai, *Nano Energy*, 2018, **47**, 210–216.
13 C. Xu, B. Li, H. Du and F. Kang, *Angew. Chem., Int. Ed.*, 2012, **51**, 933–935.
14 P. He, G. Zhang, X. Liao, M. Yan, X. Xu, Q. An, J. Liu and L. Mai, *Adv. Energy Mater.*, 2018, **8**, 1702463.
15 G. A. Elia, K. Marquardt, K. Hoeppner, S. Fantini, R. Lin, E. Knipping, W. Peters, J. F. Drillet, S. Passerini and R. Hahn, *Adv. Mater.*, 2016, **28**, 7564–7579.
16 F. Ambroz, T. J. Macdonald and T. Nann, *Adv. Energy Mater.*, 2017, **7**, 1602093.
17 M. C. Lin, M. Gong, B. Lu, Y. Wu, D. Y. Wang, M. Guan, M. Angell, C. Chen, J. Yang, B. J. Hwang and H. Dai, *Nature*, 2015, **520**, 325–328.
18 X. Zhang, G. Zhang, S. Wang, S. Li and S. Jiao, *J. Mater. Chem. A*, 2018, **6**, 3084–3090.
19 N. Jayaprakash, S. K. Das and L. A. Archer, *Chem. Commun.*, 2011, **47**, 12610–12612.
20 C. Ling and F. Mizuno, *Chem. Mater.*, 2013, **25**, 3062–3071.
21 Z. A. Zafar, S. Imtiaz, R. Razaq, S. Ji, T. Huang, Z. Zhang, Y. Huang and J. A. Anderson, *J. Mater. Chem. A*, 2017, **5**, 5646–5660.
22 H. Wang, Y. Bai, S. Chen, X. Luo, C. Wu, F. Wu, J. Lu and K. Amine, *ACS Appl. Mater. Interfaces*, 2015, **7**, 80–84.
23 M. Chiku, H. Takeda, S. Matsumura, E. Higuchi and H. Inoue, *ACS Appl. Mater. Interfaces*, 2015, **7**, 24385–24389.
24 H. Chen, F. Guo, Y. Liu, T. Huang, B. Zheng, N. Ananth, Z. Xu, W. Gao and C. Gao, *Adv. Mater.*, 2017, **29**, 1605958.
25 X. Yu, B. Wang, D. Gong, Z. Xu and B. Lu, *Adv. Mater.*, 2017, **29**, 1604118.
26 L. Zhang, L. Chen, H. Luo, X. Zhou and Z. Liu, *Adv. Energy Mater.*, 2017, **7**, 1700034.

27 Y. Hu, D. Ye, B. Luo, H. Hu, X. Zhu, S. Wang, L. Li, S. Peng and L. Wang, *Adv. Mater.*, 2017, **30**, 1703824.
28 S. Wang, S. Jiao, J. Wang, H. S. Chen, D. Tian, H. Lei and D. N. Fang, *ACS Nano*, 2017, **11**, 469–477.
29 S. Wang, Z. Yu, J. Tu, J. Wang, D. Tian, Y. Liu and S. Jiao, *Adv. Energy Mater.*, 2016, **6**, 1600137.
30 L. Geng, G. Lv, X. Xing and J. Guo, *Chem. Mater.*, 2015, **27**, 4926–4929.
31 Y. Hu, B. Luo, D. Ye, X. Zhu, M. Lyu and L. Wang, *Adv. Mater.*, 2017, **29**, 1606132.
32 L. Geng, J. Scheifers, C. Fu, J. Zhang, F. Bpt and J. Guo, *ACS Appl. Mater. Interfaces*, 2017, **9**, 21251–21257.
33 Z. Li, B. Niu, J. Liu, J. Li and F. Kang, *ACS Appl. Mater. Interfaces*, 2018, **10**, 9451–9459.
34 V. V. Kulish, D. Koch and S. Manzhos, *Phys. Chem. Chem. Phys.*, 2017, **19**, 6076–6081.
35 J. Zhou, L. Wang, M. Yang, J. Wu, F. Chen, W. Huang, H. Na, H. Ye, F. Zhao and Y. Li, *Adv. Mater.*, 2017, **29**, 1702061.
36 Z. Yu, Z. Kang, Z. Hu, J. Lu, Z. Zhou and S. Jiao, *Chem. Commun.*, 2016, **52**, 10427–10430.
37 D. Chao, C. Zhu, X. Xia, J. Liu, X. Zhang, J. Wang, P. Liang, J. Lin, H. Zhang and Z. X. Shen, *Nano Lett.*, 2015, **15**, 565–573.
38 J. Feng, X. Sun, C. Wu, L. Peng, C. Lin, S. Hu, J. Yang and Y. Xie, *J. Am. Chem. Soc.*, 2011, **133**, 17832–17838.
39 H. Wang, S. Gu, Y. Bai, S. Chen, N. Zhu, C. Wu and F. Wu, *J. Mater. Chem. A*, 2015, **3**, 22677–22686.
40 X. Zhang, S. Wang, J. Tu, G. Zhang, S. Li, D. Tian and S. Jiao, *ChemSusChem*, 2017, **11**, 705–715.
41 J. Jiang, H. Li, J. Huang, K. Li, J. Zeng, Y. Yang, J. Li, Y. Wang, J. Wang and J. Zhao, *ACS Appl. Mater. Interfaces*, 2017, **9**, 28486–28494.

